# Pressure-induced evolution of structural and electronic properties in TiTe$_2$

Yonghui Zhou,[1,*] Chunhua Chen,[1,2,*] Ying Zhou,[1,2] Xuliang Chen,[1] Chuanchuan Gu,[1] Chao An,[3] Bowen Zhang,[1,2]
Yifang Yuan,[1,2] Hao Wu,[1,4] Ranran Zhang,[1] Lili Zhang,[5] Xiangde Zhu,[1,†] Xiaoping Yang,[1,‡] and Zhaorong Yang[1,3,6,§]

[1]*Anhui Province Key Laboratory of Condensed Matter Physics at Extreme Conditions, High Magnetic Field Laboratory,
Chinese Academy of Sciences, Hefei 230031, China*
[2]*University of Science and Technology of China, Hefei 230026, China*
[3]*Institutes of Physical Science and Information Technology, Anhui University, Hefei 230601, China*
[4]*Department of Physics and Laboratory of Material Physics, Zhengzhou University, Zhengzhou 450052, China*
[5]*Shanghai Synchrotron Radiation Facility, Shanghai Advanced Research Institute,
Chinese Academy of Sciences, Shanghai 201204, China*
[6]*Collaborative Innovation Center of Advanced Microstructures, Nanjing University, Nanjing 210093, China*

Bulk 1$T$-TiTe$_2$ (hexagonal, space group $P$-3$m$1) exhibits semimetallic conductivity with weak Anderson localization characteristic at ambient pressure, but superconductivity under high pressure of $\sim$5 GPa. Here the detailed evolutions of structural and transport properties in TiTe$_2$ during compression are investigated by extending pressure up to 50.2 GPa. The combined high-pressure electrical transport and synchrotron x-ray diffraction experiments unravel two critical pressure points. At $P_{c1} \sim 5.4$ GPa, the superconductivity emerges, which is accompanied by a structural transition from $P$-3$m$1 to a mixture of $P$-3$m$1 and monoclinic $C2/m$ phase. The localization effect maintains until the structural transition is over at $P_{c2} \sim 19.1$ GPa, meanwhile the Hall coefficient $R_H$ changes from positive to negative. Our results demonstrate that the superconductivity in the pressurized TiTe$_2$ can be assigned to the high-pressure $C2/m$ phase which is electron dominated.

Layered transition metal dichalcogenides have attracted extensive interest due to their rich physical properties [1–9] and wide applications in two-dimensional devices [10–12]. Among them, titanium dichalcogenides Ti$X_2$($X =$ S, Se, Te) have received attention mainly focusing on their exotic properties such as charge-density wave (CDW), superconductivity, and topological phase transition [13–27]. The Ti$X_2$ crystallizes in a hexagonal CdI$_2$-type structure with Ti$X_6$ octahedron, namely 1$T$ phase, where the adjacent $X$-Ti-$X$ sandwiches with van der Waals interactions. While TiS$_2$ is a semiconductor with a gap of $\sim$0.18 eV, TiSe$_2$ is a narrow-band-gap indirect semiconductor and exhibits a commensurate CDW transition at $\sim$200 K [28]. The transition temperature of CDW is enhanced to $\sim$232 K via thinning the sample to nanometer [23]. Moreover, both Cu intercalation and application of pressure in the TiSe$_2$ lead to the appearance of superconductivity [16,29]. In contrast, TiTe$_2$ behaves as a semimetal due to the partial overlap of Te-5$p$ and Ti-3$d$ bands, which has been identified as a prototype of Fermi liquid [30–32]. Although bulk TiTe$_2$ excludes the CDW instability or superconducting transition down to 0.45 K due to weak electron-phonon coupling [33–35], the emergence of CDW was reported in the single layer [27]. Very recently it was theoretically predicted that the TiTe$_2$ undergoes a series of topological phase

transitions under high hydrostatic pressure or strain [26]. Soon after, two topological phase transitions, followed by a structural phase transition at $\sim$8 GPa from hexagonal $P$-3$m$1 to a mixture phase of $P$-3$m$1 and monoclinic $C2/m$, were experimentally confirmed by combined high-pressure synchrotron x-ray diffraction (XRD) and Raman spectroscopy [36–38]. Meanwhile, Dutta *et al.* reported the observation of superconductivity at $\sim$5 GPa [37]. However, because the maximum pressure applied in the XRD and Hall resistivity measurements is below 20 GPa, the detailed correlation between structure and superconductivity as well as their evolutions under pressure is still unclear.

Here we investigate the structural and electronic properties of TiTe$_2$ by performing high-pressure electrical transport and synchrotron XRD experiments up to 50.2 GPa. We show that the structural transition from hexagonal $P$-3$m$1 to monoclinic $C2/m$ phase starts at $P_{c1} \sim 5.4$ GPa and finishes at $P_{c2} \sim$ 19.1 GPa. The superconductivity emerges around $P_{c1}$, and is robust up to 50.2 GPa. At $P_{c2}$, accompanied by the completion of structural transition, the dominant carrier changes from hole to electron together with complete suppression of weak localization in the low-temperature region. These results consistently suggest that the emergent superconductivity originates from the high-pressure monoclinic phase which is electron dominated.

Experimental details are presented in Supplemental Material [39]. As illustrated in Supplemental Material, Fig. S1(a), bulk TiTe$_2$ crystallizes in the layered CdI$_2$-type structure with space group $P$-3$m$1 (No. 164, 1$T$ phase), where the Ti and Te atoms locate at 1$a$(0, 0, 0) and 2$d$(1/3, 2/3, 0.2628) Wyckoff

---

*These authors contributed equally to this work.
†xdzhu@hmfl.ac.cn
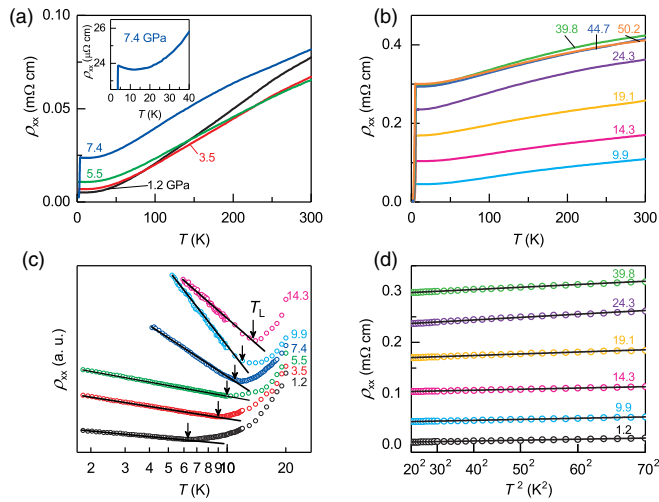‡xpyang@hmfl.ac.cn
§zryang@issp.ac.cn

FIG. 1. In-plane longitudinal resistivity of $TiTe_2$ single crystal as a function of temperature under various pressures in run 1. (a) Electrical resistivity curves at low pressures. Inset: Enlarged view of low-temperature resistivity curve at 7.4 GPa, suggesting the coexistence of weak localization and pressure-induced superconductivity. (b) Electrical resistivity curves from 9.9 to 50.2 GPa. (c) Electrical resistivity curves below 20 K on a semilogarithmic scale, suggesting the evolution of weak localization temperature $T_L$ as indicated by the arrows. For clarity, the resistivity curves here are offset. (d) Electrical resistivity vs $T^2$ between 20 and 70 K, following a Fermi liquid behavior. Black solid lines in (c), (d) denote the fitting curves.



FIG. 2. Pressure-induced superconductivity and upper critical field in $TiTe_2$ under pressure. (a) Electrical resistivity curves around superconducting transition temperature up to 50.2 GPa. (b), (c) Temperature dependence of resistivity under different magnetic fields perpendicular to the *ab* plane at 24.3 and 44.7 GPa, respectively. (d) Temperature dependence of the upper critical field $\mu_0 H_{c2}$ at 24.3 and 44.7 GPa, respectively. $T_c$ is determined as 90% drop of the normal-state resistance. Red solid lines represent the Ginzburg-Landau fitting.

sites, respectively [51]. Figure S1(b) shows the single-crystal XRD patterns which display only *(00l)* diffraction peaks, reflecting a *c*-axis orientation growth. The Rietveld analysis of powder XRD patterns indicates the pure hexagonal *P*-3*m*1 phase. The resulting lattice parameter is $a = 3.767$ Å, $c = 6.498$ Å, in good agreement with the previous report [30]. Figure S1(c) shows the energy-dispersive x-ray spectroscopy characterization, suggesting the composition of $TiTe_{1.99}$ with 0.5% Te deficiency. These results confirm the high quality of the sample used here. Figure S1(d) shows temperature dependence of the renormalized *ab*-plane resistivity in three pieces of samples from different batches. The residual resistivity ratio ($\rho_{300\,K}/\rho_{5\,K}$) was estimated to be 18.6, 19.1, and 14.1, respectively. All samples exhibit metallic behavior upon cooling followed by a small upturn below $T_L \sim 6$ K [see Fig. S1(d)]. The upturned resistivity displays a log$T$ dependence, as shown in the inset of Fig. S1(d), which is consistent with the experimental results of Ref. [33]. Considering that $TiTe_2$ is a trivial semimetal as a prototype of Fermi liquid at ambient pressure [26,31,32], this log$T$-dependent resistivity upturn could be attributed to the weak Anderson localization due to the presence of disorder or vacancy [33]. It was suggested that two types of charge carriers coexist in $TiTe_2$, i.e., three-dimensional (3D) hole and two-dimensional (2D) electron pockets, and the 2D electrons would then undergo the Anderson localization at low temperature [33].

Figure 1(a) shows the longitudinal resistivity curves $\rho_{xx}(T)$ of $TiTe_2$ single crystal under high pressure (run 1). At 1.2 GPa, the $\rho(T)$ curve is very similar to that at ambient pressure, i.e., overall metallic with small upturn of resistivity
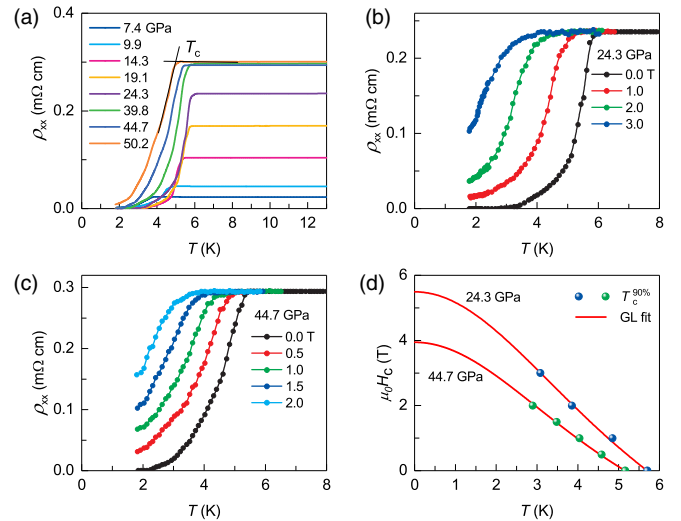
in the low-temperature region. With increasing pressure, a steep resistive drop is observed at ∼3.8 K and 7.4 GPa, which is indicative of a superconducting transition and consistent with a recent report [37]. Zero-resistance conductivity is achieved at 9.9 GPa, and the superconductivity is robust upon compression up to 50.2 GPa, the maximum pressure studied in this work [see Figs. 1(b) and 2(a)]. As seen from the semilogarithmic plot of the resistance in Fig. 1(c), the weak Anderson localization dominates with increasing pressure up to 14.3 GPa, with the localization temperature $T_L$ shifting monotonically to higher temperatures. Although the Raman spectra of Ref. [36] suggested electron-phonon coupling in the ambient phase of $TiTe_2$, our temperature-dependent resistivity curves behave as a Fermi liquid behavior $\rho \sim T^2$ between 20 and 70 K as shown in Fig. 1(d), indicative of the dominate electron-electron interactions.

To check the critical magnetic field of the superconducting $TiTe_2$, we performed electrical transport measurements under various external magnetic fields perpendicular to the *ab* plane. At 24.3 GPa, the superconducting transition is gradually suppressed by the increasing magnetic field, as shown in Fig. 2(b). By defining $T_c$ with the resistance criterion of $R_{cri} = 90\% R_n$ ($R_n$ is the normal-state resistance), we constructed the temperature–magnetic field phase diagram in Fig. 2(d). The data can be well fitted by the Ginzburg-Landau formula [52], $\mu_0 H_{c2}(T) = \mu_0 H_{c2}(0)(1 - t^2)/(1 + t^2)$, where $t$ denotes a reduced temperature of $T/T_c$. The fitting yields a critical field $\mu_0 H_{c2}(0)$ of 5.493 T, which is much lower than the Pauli limiting field $\mu_0 H_P(0) = 1.84 T_c = 10.488$ T [53]. According to the relationship $\mu_0 H_{c2} = \Phi_0/(2\pi \xi^2)$, where $\Phi_0 = 2.07 \times 10^{-15}$ Wb is the flux quantum, the coherence length $\xi_{GL}(0)$ of

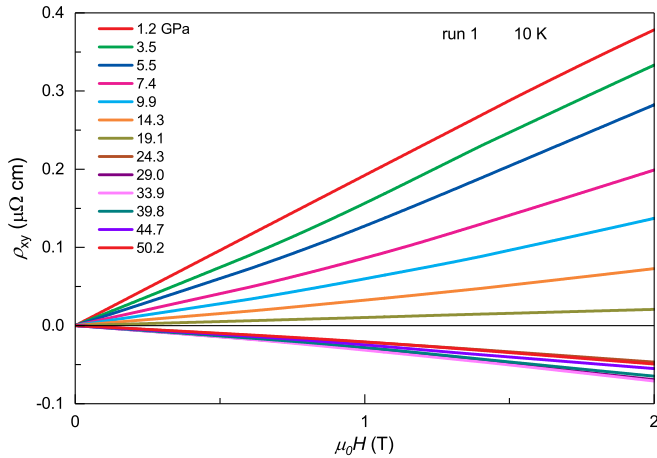FIG. 3. Hall resistivity $\rho_{xy}$ of TiTe$_2$ as a function of applied magnetic field perpendicular to the $ab$ plane at 10 K up to 50.2 GPa in run 1. Hall resistivity curves display a positive slope below 19.1 GPa and a negative slope above 19.1 GPa.

243 Å is obtained. For 44.7 GPa as shown in Figs. 2(c) and 2(d), the critical field $\mu_0 H_{c2}$ and correlation length $\xi_{GL}(0)$ are 3.943 T and 287 Å, respectively. Since the coherence length is greater than the interlayer separation, the superconductivity is of 3D in nature.

To further study the evolution of the charge carriers under pressure, Hall measurements were carried out at 10 K and various pressures. Figure 3 displays the transversal Hall resistivity $\rho_{xy}$ as a function of magnetic field perpendicular to the $ab$ plane of sample. For 1.2 GPa, the positive slope of $\rho_{xy}(H)$ curve indicates that hole-type carriers dominate the transport behavior of hexagonal TiTe$_2$, in agreement with previous report [33]. The Hall coefficient $R_H$, extracted from the slope of $\rho_{xy}(H)$, decreases monotonically with increasing pressure and changes from positive to negative above 19.1 GPa. After reaching a negative maximum around 29.0 GPa, the $R_H$ turns back to increase. The sign change of the $R_H$ indicates clearly that the hole-dominated behavior maintains up to 19.1 GPa, and transforms into electron dominated at higher pressures.

For comparison, we further carried out transport measurements without using pressure medium in the second run, which is referred as nonhydrostatic pressure similar to that of Ref. [37]. In general, the $\rho(T)$ curves up to 30.0 GPa are qualitatively consistent with that of quasihydrostatic pressure condition in Fig. 1, indicating the reproducibility of weak localization, superconductivity, and sign-reversal Hall slope (see Fig. S2). Note that no trace of CDW-like feature can be recognized from these resistivity curves within the experimental resolution, which is somewhat different from the case of Ref. [37].

To explore the thermodynamic stability of the pristine 1$T$-TiTe$_2$ phase under high pressure and the correlation between structural properties and electronic properties, we further performed synchrotron powder XRD measurements at room temperature up to 40.0 GPa. Pristine 1$T$-TiTe$_2$ crystallizes in a hexagonal structure with the space group $P$-3$m$1 at ambient pressure. After applying external pressure
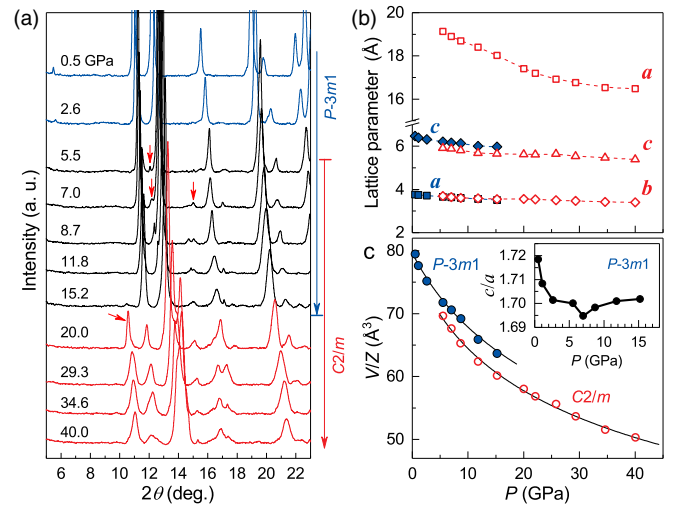


FIG. 4. High-pressure synchrotron powder x-ray diffraction patterns of TiTe$_2$ at room temperature ($\lambda = 0.6199$ Å). (a) Representative diffraction patterns from 0.5 to 40.0 GPa. (b) Pressure-dependent lattice parameters $a$, $b$, and $c$. (c) Unit-cell volume per formula unit ($V/Z$) as a function of pressure. Solid and open circles denote the hexagonal ($P$-3$m$1, $Z = 1$) and monoclinic ($C2/m$, $Z = 6$) phases, respectively. Structural phase transition leads to a contraction of the unit-cell volume of about 3.0% at 5.5 GPa. Solid lines are the fitting result based on the third-order Birch-Murnaghan equation of state. Inset: $c/a$ ratio as a function of pressure in the 1$T$-TiTe$_2$ phase ($P$-3$m$1).

of 0.5 GPa, the diffraction pattern can be well refined by the space group of $P$-3$m$1 [see Fig. S3(a)]. As shown in Fig. 4(a), diffraction peaks indicated by arrows start to appear with increasing pressure up to 5.5 GPa, which suggests the presence of structural phase transition. With increasing pressure up to 20.0 GPa, a peak appearing at around 10.5° becomes prominent and shifts towards higher angles upon further compression until 40.0 GPa. We have conducted the structure prediction using USPEX to determine the high-pressure phase [39]. The enthalpy-pressure curves plotted in Fig. S4 indicate that monoclinic $C2/m$ has the lowest enthalpy above 10 GPa. Note that the structure prediction is in agreement with the experimental results of Ref. [36], which suggested a possible structural transition from hexagonal $P$-3$m$1 to monoclinic $C2/m$ phase around 8 GPa. Consistently, all the patterns above 20.0 GPa can be well refined by the space group of $C2/m$ (No. 12), confirming the stability of the high-pressure monoclinic phase. Representative Le Bail refinements of the XRD patterns at 0.5, 7.0, 15.2, and 40.0 GPa are shown in Fig. S3, respectively. The lattice parameters $a$, $b$, and $c$ are displayed in Fig. 4(b). The unit-cell volume as a function of pressure can be fitted by the third-order Birch-Murnaghan equation of state [see Fig. 4(c)] [54]. The fitting results yield the ambient pressure volume $V_0 = 79.63$ Å$^3$, bulk modulus $B_0 = 45.3$ GPa and its first pressure derivative $B_0' = 4.0$ for the low-pressure hexagonal phase, and $V_0 = 78.77$ Å$^3$, $B_0 = 31.3$ GPa, and $B_0' = 4.6$ for the high-pressure monoclinic phase. The structural phase transition leads to a contraction of the unit-cell volume of about 3.0% at 5.5 GPa. For the case of $P$-3$m$1 phase, the pressure-dependent $c/a$ ratio plotted
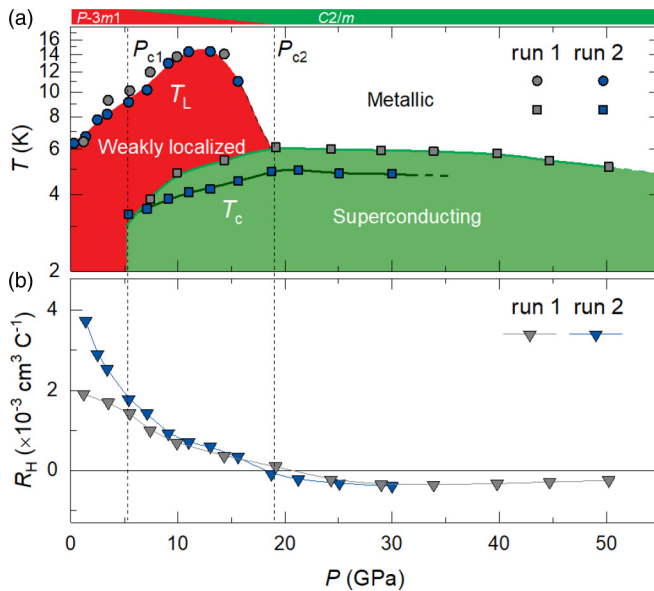
FIG. 5. Temperature-pressure phase diagram of TiTe$_2$ compound and pressure-dependent carrier density and mobility under quasihydrostatic (run 1) and nonhydrostatic (run 2) pressure, respectively. (a) Gray (blue) circles and squares represent $T_L$ and $T_c$ values extracted from the longitudinal resistivity measurements of run 1 (run 2). $T_L$ corresponds to the weakly localized temperature, below which the resistivity is proportional to log$T$. $T_c$ is determined as the onset temperature of superconducting transition. For clarity, the vertical axis here is on a semilogarithmic scale. Colored areas are guides to the eyes, indicating the metallic, weakly localized, and superconducting phases, respectively. The dashed line around 5.5 GPa indicates the critical pressure $P_{c1}$, concomitant with the structural phase transition from hexagonal $P$-3$m$1 to monoclinic $C2/m$ phase deduced from Fig. 4(c). (b) Pressure-dependent Hall coefficient $R_H$ at 10 K in run 1 and run 2, respectively. The change of dominant carriers from holes to electrons appears around a critical pressure $P_{c2}$ of $\sim$19.1 GPa, in line with the end of the structural phase transition from hexagonal $P$-3$m$1 to monoclinic $C2/m$ phase.

in the inset of Fig. 4(c) changes slopes around 2.6 GPa and shows discontinuity around 7.0 GPa, roughly consistent with the results of Ref. [36]. The anomaly around 2.6 GPa could be ascribed to the transition from 2D to 3D [36], and the discontinuity around 7.0 GPa might be attributed to a coexistence of structural phase transition and electronic topological transition (ETT). In line with the possible existence of ETT, the resistivity at room temperature displays a minimum around 6–7 GPa (see Fig. S5) [55,56]. After releasing to ambient pressure, the pressurized sample restores to the initial hexagonal phase, which is consistent with the recovered semimetallic conductivity upon decompression to 1.0 GPa (see Fig. S6).

A comprehensive temperature-pressure phase diagram for TiTe$_2$ compound is summarized in Fig. 5(a), from which two critical pressure points can be discerned. At the first critical pressure $P_{c1} \sim 5.4$ GPa the superconductivity emerges, accompanied by the structural transition from hexagonal $P$-3$m$1 to monoclinic $C2/m$ phase. The monoclinic $C2/m$ mixes

with the original $P$-3$m$1 until the second critical pressure $P_{c2}$ of $\sim$19.1 GPa. When the structural transition finishes at $P_{c2}$, the superconducting transition temperature $T_c$ reaches a maximum, meanwhile the Hall coefficient $R_H$ changes from positive to negative as shown in Fig. 5(b). The reflection of structural evolution on the transport properties could also be traced by the pressure dependence of $T_L$. As seen from Fig. 5(a), $T_L$ first increases with pressure then decreases sharply beyond 13.0 GPa, and nearly disappears at $\sim$19.0 GPa by extrapolation.

At ambient pressure, the hexagonal TiTe$_2$ is hole dominated with localization characteristic at low temperatures. Upon compression, not only the hole-dominated behavior but also the localization effect manifests up to $P_{c2}$. Only when the hexagonal $P$-3$m$1 disappears completely, the localization effect is suppressed with the conduction type changing to electron dominated simultaneously. Clearly, the localization effect as well as hole-dominated behavior is concomitant with the hexagonal $P$-3$m$1, all of those have nothing to do with the superconductivity. In other words, the superconductivity is inherent to the high-pressure monoclinic $C2/m$ phase which is electron dominated. The electron-dominating behavior in the superconducting TiTe$_2$ is reminiscent of the Cu-intercalated $1T$-TiSe$_2$, in which the superconductivity is induced via electron doping [29].

In conclusion, the relationship of structure and charge-carrier transport properties in TiTe$_2$ compound have been investigated by combined high-pressure synchrotron XRD and electrical transport experiments. We demonstrate that the pressure-induced superconductivity can be correlated with the structural transition from hexagonal $P$-3$m$1 to monoclinic $C2/m$ phase at $P_{c1} \sim 5.4$ GPa. The mixture of $P$-3$m$1 and $C2/m$ phase between $P_{c1}$ and $P_{c2}$ leads to the coexistence of superconductivity with weak localization as well as hole-dominated transport behavior. The superconductivity in the electron-dominated monoclinic phase is robust up to 50.2 GPa. These findings will shed light on the understanding of emergent superconductivity in pressurized transition metal dichalcogenides.

[1] J. A. Wilson, F. J. Di Salvo, and S. Mahajan, Adv. Phys. **24**, 117 (1975).

[2] T. Valla, A. V. Fedorov, P. D. Johnson, J. Xue, K. E. Smith, and F. J. DiSalvo, Phys. Rev. Lett. **85**, 4759 (2000).

[3] E. Revolinsky, E. P. Lautenschlager, and C. H. Armitage, Solid State Commun. **1**, 59 (1963).

[4] B. Sipos, A. F. Kusmartseva, A. Akrap, H. Berger, L. Forro, and E. Tutis, Nat. Mater. **7**, 960 (2008).

[5] J. Kuneš, L. Baldassarre, B. Schächner, K. Rabia, C. A. Kuntscher, D. M. Korotin, V. I. Anisimov, J. A. McLeod, E. Z. Kurmaev, and A. Moewes, Phys. Rev. B **81**, 035122 (2010).

[6] A. P. Nayak, S. Bhattacharyya, J. Zhu, J. Liu, X. Wu, T. Pandey, C. Jin, A. K. Singh, D. Akinwande, and J.-F. Lin, Nat. Commun. **5**, 3731 (2014).

[7] A. P. Nayak, Z. Yuan, B. Cao, J. Liu, J. Wu, S. T. Moran, T. Li, D. Akinwande, C. Jin, and J.-F. Lin, ACS Nano **9**, 9117 (2015).

[8] Z. Zhao, H. Zhang, H. Yuan, S. Wang, Y. Lin, Q. Zeng, G. Xu, Z. Liu, G. K. Solanki, K. D. Patel, Y. Cui, H. Y. Hwang, and W. L. Mao, Nat. Commun. **6**, 7312 (2015).

[9] X. Wang, X. Chen, Y. Zhou, C. Park, C. An, Y. Zhou, R. Zhang, C. Gu, W. Yang, and Z. Yang, Sci. Rep. **7**, 46694 (2017).

[10] Q. H. Wang, K. Kalantar-Zadeh, A. Kis, J. N. Coleman, and M. S. Strano, Nat. Nanotechnol. **7**, 699 (2012).

[11] G. R. Bhimanapati, Z. Lin, V. Meunier, Y. Jung, J. Cha, S. Das, D. Xiao, Y. Son, M. S. Strano, V. R. Cooper, L. Liang, S. G. Louie, E. Ringe, W. Zhou, S. S. Kim, R. R. Naik, B. G. Sumpter, H. Terrones, F. Xia, Y. Wang, J. Zhu, D. Akinwande, N. Alem, J. A. Schuller, R. E. Schaak, M. Terrones, and J. A. Robinson, ACS Nano **9**, 11509 (2015).

[12] K. S. Novoselov, A. Mishchenko, A. Carvalho, and A. H. Castro Neto, Science **353**, aac9439 (2016).

[13] C. M. Fang, R. A. de Groot, and C. Haas, Phys. Rev. B **56**, 4455 (1997).

[14] K. Rossnagel, L. Kipp, and M. Skibowski, Phys. Rev. B **65**, 235101 (2002).

[15] A. H. Reshak and S. Auluck, Phys. Rev. B **68**, 245113 (2003).

[16] A. F. Kusmartseva, B. Sipos, H. Berger, L. Forró, and E. Tutiš, Phys. Rev. Lett. **103**, 236401 (2009).

[17] J. van Wezel, P. Nahai-Williamson, and S. S. Saxena, Phys. Rev. B **81**, 165109 (2010).

[18] M. M. May, C. Brabetz, C. Janowitz, and R. Manzke, Phys. Rev. Lett. **107**, 176405 (2011).

[19] M. Iavarone, R. Di Capua, X. Zhang, M. Golalikhani, S. A. Moore, and G. Karapetrov, Phys. Rev. B **85**, 155103 (2012).

[20] B. Zenker, H. Fehske, H. Beck, C. Monney, and A. R. Bishop, Phys. Rev. B **88**, 075138 (2013).

[21] R. Claessen, T. Straub, P. Steiner, S. Hüfner, V. Eyert, R. O. Anderson, J. W. Allen, C. Janowitz, and C. G. Olson, Physica B **230-232**, 294 (1997).

[22] Y. I. Joe, X. M. Chen, P. Ghaemi, K. D. Finkelstein, G. A. de la Pena, Y. Gan, J. C. T. Lee, S. Yuan, J. Geck, G. J. MacDougall, T. C. Chiang, S. L. Cooper, E. Fradkin, and P. Abbamonte, Nat. Phys. **10**, 421 (2014).

[23] P. Chen, Y. H. Chan, X. Y. Fang, Y. Zhang, M. Y. Chou, S. K. Mo, Z. Hussain, A. V. Fedorov, and T. C. Chiang, Nat. Commun. **6**, 8943 (2015).

[24] G. Nicolay, B. Eltner, S. Hüfner, F. Reinert, U. Probst, and E. Bucher, Phys. Rev. B **73**, 045116 (2006).

[25] V. N. Strocov, E. E. Krasovskii, W. Schattke, N. Barrett, H. Berger, D. Schrupp, and R. Claessen, Phys. Rev. B **74**, 195125 (2006).

[26] Q. Zhang, Y. Cheng, and U. Schwingenschlögl, Phys. Rev. B **88**, 155317 (2013).

[27] P. Chen, W. W. Pai, Y. H. Chan, A. Takayama, C. Z. Xu, A. Karn, S. Hasegawa, M. Y. Chou, S. K. Mo, A. V. Fedorov, and T. C. Chiang, Nat. Commun. **8**, 516 (2017).

[28] F. J. Di Salvo, D. E. Moncton, and J. V. Waszczak, Phys. Rev. B **14**, 4321 (1976).

[29] E. Morosan, H. W. Zandbergen, B. S. Dennis, J. W. G. Bos, Y. Onose, T. Klimczuk, A. P. Ramirez, N. P. Ong, and R. J. Cava, Nat. Phys. **2**, 544 (2006).

[30] D. K. G. de Boer, C. F. van Bruggen, G. W. Bus, R. Coehoorn, C. Haas, G. A. Sawatzky, H. W. Myron, D. Norman, and H. Padmore, Phys. Rev. B **29**, 6797 (1984).

[31] R. Claessen, R. O. Anderson, J. W. Allen, C. G. Olson, C. Janowitz, W. P. Ellis, S. Harm, M. Kalning, R. Manzke, and M. Skibowski, Phys. Rev. Lett. **69**, 808 (1992).

[32] L. Kipp, K. Roßnagel, C. Solterbeck, T. Strasser, W. Schattke, and M. Skibowski, Phys. Rev. Lett. **83**, 5551 (1999).

[33] Y. Koike, M. Okamura, T. Nakanomyo, and T. Fukase, J. Phys. Soc. Jpn. **52**, 597 (1983).

[34] P. B. Allen and N. Chetty, Phys. Rev. B **50**, 14855 (1994).

[35] L. Perfetti, C. Rojas, A. Reginelli, L. Gavioli, H. Berger, G. Margaritondo, M. Grioni, R. Gaál, L. Forró, and F. Rullier Albenque, Phys. Rev. B **64**, 115102 (2001).

[36] V. Rajaji, U. Dutta, P. C. Sreeparvathy, S. C. Sarma, Y. A. Sorb, B. Joseph, S. Sahoo, S. C. Peter, V. Kanchana, and C. Narayana, Phys. Rev. B **97**, 085107 (2018).

[37] U. Dutta, P. S. Malavi, S. Sahoo, B. Joseph, and S. Karmakar, Phys. Rev. B **97**, 060503(R) (2018).

[38] M. Zhang, X. Wang, A. Rahman, Q. Zeng, D. Huang, R. Dai, Z. Wang, and Z. Zhang, Appl. Phys. Lett. **112**, 041907 (2018).

[39] See Supplemental Material at http://link.aps.org/supplemental/10.1103/PhysRevB.99.125104 for the experimental details and the supporting data, which includes Refs. [40–50].

[40] P. C. Canfield and I. R. Fisher, J. Cryst. Growth **225**, 155 (2001).

[41] H. K. Mao, J. Xu, and P. M. Bell, J. Geophys. Res. **91**, 4673 (1986).

[42] C. Prescher and V. B. Prakapenka, High Press. Res. **35**, 223 (2015).

[43] A. C. Larsen and R. B. Von Dreele, General Structure Analysis System (GSAS), Los Alamos 29 National Laboratory Report LAUR, 86-748 (2000)

[44] A. R. Oganov and C. W. Glass, J. Chem. Phys. **124**, 244704 (2006).

[45] A. O. Lyakhov, A. R. Oganov, H. T. Stokes, and Q. Zhu, Comput. Phys. Commun. **184**, 1172 (2013).

[46] G. Kresse and J. Hafner, Phys. Rev. B **47**, 558 (1993).

[47] G. Kresse and J. Furthmüller, Phys. Rev. B **54**, 11169 (1996).

[48] J. P. Perdew, K. Burke, and M. Ernzerhof, Phys. Rev. Lett. **77**, 3865 (1996).

[49] G. Kresse and D. Joubert, Phys. Rev. B **59**, 1758 (1999).

[50] P. E. Blöchl, Phys. Rev. B **50**, 17953 (1994).

[51] Y. Arnaud and M. Chevreton, J. Solid State Chem. **39**, 230 (1981).

[52] V. L. Ginzburg and L. D. Landau, Zh. Eksp. Teor. Fiz. **20**, 1064 (1950).

[53] A. M. Clogston, Phys. Rev. Lett. **9**, 266 (1962).

[54] F. Birch, Phys. Rev. **71**, 809 (1947).

[55] V. Rajaji, P. S. Malavi, S. S. R. K. C. Yamijala, Y. A. Sorb, U. Dutta, S. N. Guin, B. Joseph, S. K. Pati, S. Karmakar, K. Biswas, and C. Narayana, Appl. Phys. Lett. **109**, 171903 (2016).

[56] Y. A. Sorb, V. Rajaji, P. S. Malavi, U. Subbarao, P. Halappa, S. C. Peter, S. Karmakar, and C. Narayana, J. Phys.: Condens. Matter **28**, 015602 (2016).